Materials Advances

ROYAL SOCIETY OF CHEMISTRY

PAPER

View Article Online
View Journal | View Issue

Cite this: *Mater. Adv.*, 2026, 7, 2911

A robust, multifunctional optical sensing platform operating under practical conditions

Ikhlas Kachou,[a] Mouna Fhoula,[a] Kamel Saidi,[ab] Christian Hernández-Álvarez,[d] Mohamed Dammak *[a] and Inocencio R. Martín [c]

This work presents a systematic investigation of $Ho^{3+}/Tm^{3+}/Yb^{3+}$ tri-doped $LiCaLa(MoO_4)_3$ (LCLMO) phosphors as an optical platform for ratiometric thermometry. The LCLMO host lattice combines low phonon energy, high thermal stability, and a tunable crystal field environment, enabling efficient energy transfer among the incorporated lanthanide ions. Under continuous-wave excitation at 975 nm, Yb^{3+} ions act as effective sensitizers, transferring excitation energy non-radiatively to Ho^{3+} and Tm^{3+} activators and generating intense multicolor upconversion emissions spanning the visible and NIR spectral regions. Temperature sensing performance was evaluated using four optimized fluorescence intensity ratio (FIR) pairs, including one thermally coupled ($FIR_{700/795}$) and three non-thermally coupled channels ($FIR_{700/477}$, $FIR_{700/660}$, and $FIR_{700/550}$), providing redundant and reliable temperature readout. A high relative sensitivity of 3.22% K^{-1} at 298 K was achieved, accompanied by excellent temperature resolution (ΔT = 0.8 K) over a broad operating range of 298–588 K. The combination of high thermometric sensitivity, multi-channel ratiometric reliability, extended temperature operability, and NIR excitation establishes LCLMO:$Ho^{3+}/Tm^{3+}/Yb^{3+}$ phosphors as a promising multifunctional platform for advanced luminescent thermometry and optical sensing.

Received 18th January 2026,
Accepted 4th February 2026

DOI: 10.1039/d6ma00079g

rsc.li/materials-advances

Introduction

Researchers are increasingly concentrating on rare-earth ion-doped phosphors due to their excellent optical features, including great chemical stability, intrinsic resistance to photodegradation, and strong brightness.[1–6] These materials have proven indispensable in different applications such as optical thermometry, and photothermal therapy, where precise, non-invasive temperature measurement is critical without compromising target tissue integrity.[7,8] While 975 nm laser excitation can be advantageous in terms of reduced scattering and improved light propagation in complex media, two key hurdles persist: laser-induced thermal heating and the inherently limited upconversion luminescence efficiency. In contrast, near-infrared upconversion provides major advantages over conventional downshifting fluorescence approaches. The use of NIR excitation enables more effective light delivery through optically turbid environments compared to short-wavelength UV-visible excitation commonly required for traditional fluorophores. Additionally, upconversion materials typically exhibit narrower emission bands and reduced background interference, resulting in improved signal-to-noise ratios for optical sensing and luminescence-based readout.[9–11]

Molybdate-based compounds have become notably significant as hosts for upconversion applications, due to the favorable structural features of $(MoO_4)^{2-}$ tetrahedra. These structural units generate significant local asymmetry, thereby increasing the transition probability for the theoretically prohibited 4f–4f electronic transitions and consequently improving upconversion efficiency. The presence of heavy Mo^{6+} cations further facilitates phonon-assisted energy transfer mechanisms while concurrently diminishing non-radiative multiphonon relaxation pathways, attributable to the inherently low phonon energy of the molybdate lattice. Together, these characteristics establish Mo-based host matrices as exceptional substrates for producing stable, tunable near-infrared upconversion emissions, rendering them ideally adapted for advanced thermal sensing applications.

Among lanthanide-doped molybdates, the $LiCaLa(MoO_4)_3$ (LCLMO) host lattice has garnered considerable attention for photonic applications owing to its exceptional chemical and thermal stability, broad optical bandgap, and highly efficient luminescence. The LCLMO structure is especially notable for its

[a] *Laboratoire de Physique Appliquée, Faculté des Sciences de Sfax, Département de Physique, Université de Sfax, BP 1171 Sfax, Tunisia. E-mail: mohamed.dammak@fss.usf.tn, madidammak@yahoo.fr*
[b] *Department of Physics, Sfax Preparatory Engineering Institute, University of Sfax, 1172 – 3000 Sfax, Tunisia*
[c] *Universidad de La Laguna, Departamento de Física, MALTA-Consolider Team, IMN and IUdEA Apdo. Correos 456, E-38206 San Cristóbal de La Laguna, Santa Cruz de Tenerife, Spain*
[d] *Adam Mickiewicz University, Faculty of Chemistry, Uniwersytetu Poznańskiego 8, 61-614 Poznań, Poland*

exceptionally low phonon energy, remarkable thermal stability, and adaptable crystal field environment characteristics resulting from the synergistic interaction of mixed Li^+, Ca^{2+}, and La^{3+} coordinating ions. These structural features facilitate highly efficient and robust energy transfer between dopant ions while concurrently minimizing non-radiative decay pathways, thereby optimizing upconversion luminescence efficiency.[12–15]

The purposeful insertion of many lanthanide ions into a single host lattice provides a well-established and extremely effective technique for manufacturing spectrally-rich, tunable emissions *via* carefully regulated energy transfer processes. Specifically, the incorporation of Ho^{3+}, Tm^{3+}, and Yb^{3+} ions into the LCLMO framework provides a synergistic luminous response directed by well-defined upconversion routes. Under near-infrared stimulation (975–980 nm), Yb^{3+} ions operate as efficient initial sensitizers due to their unusually large NIR absorption cross-section. Following photon absorption, Yb^{3+} ions convey the accumulated excitation energy non-radiatively to Ho^{3+} and Tm^{3+} activator ions *via* known $Yb^{3+} \rightarrow Ho^{3+}$ and $Yb^{3+} \rightarrow Tm^{3+}$ energy transfer routes. This sequential energy transfer process populates many excited electronic states in both activator ions, providing characteristic multicolor emissions spanning the blue, green, red, and near-infrared spectrum ranges.[12,16–18]

This study investigates $Ho^{3+}/Tm^{3+}/Yb^{3+}$-doped $LiCaLa(MoO_4)_3$ phosphors as multifunctional luminescent platforms for precise optical thermometry and near-infrared (NIR) optical sensing. Benefiting from the intrinsic properties of the LCLMO host lattice including low phonon energy, high thermal stability, and a tunable crystal field environment together with efficient energy transfer among Yb^{3+} sensitizers and Ho^{3+}/Tm^{3+} activators, this work addresses key challenges in the development of high-performance luminescent materials for non-invasive and real-time temperature monitoring. The synergistic upconversion behavior of the tri-doped system enables robust ratiometric temperature readout and NIR-excited optical detection, highlighting its potential for multifunctional sensing and photonic applications. To elucidate structure property relationships and optimize thermometric performance, a comprehensive investigation encompassing material synthesis, phase and structural analysis, detailed optical spectroscopy, and systematic thermometric evaluation is carried out, providing insight into the energy transfer processes governing the luminescence response.

Synthesis of LCLMO doped $Ho^{3+}/Tm^{3+}/Yb^{3+}$

$LiCaLa(MoO_4)_3$ (LCLMO) samples doped with Ho^{3+}, Tm^{3+}, and Yb^{3+} ions were synthesized *via* a conventional solid-state reaction method. Analytical-grade precursor materials MoO_3 (99.99%), Li_2CO_3 (99.99%), $CaCO_3$ (99.99%), La_2O_3 (99.99%), Ho_2O_3 (99.99%), Tm_2O_3 (99.99%), and Yb_2O_3 (99.99%) were weighed in stoichiometric proportions corresponding to the nominal composition $Li_1Ca_1La_{1-x-y-z}MoO_4$ (where $x = 0.01$ for Ho^{3+}, $y = 0.01$ for Tm^{3+}, $z = 0.15$ for Yb^{3+}, expressed in molar percentages). The precursor powders were thoroughly homogenized by grinding in an agate mortar for 60 minutes to ensure uniform mixing and particle size reduction. The resulting mixture was transferred into a high-purity alumina crucible and subjected to an initial calcination step at 800 °C for 5 hours with a heating rate of 5 °C min^{-1} in air. Following natural cooling to room temperature, the calcined powder was recovered, finely ground for 30 minutes in an agate mortar, and subsequently subjected to a high-temperature sintering treatment at 950 °C for 8 hours with an identical heating rate of 5 °C min^{-1}. The furnace was again allowed to cool naturally to room temperature without forced quenching or rapid cooling protocols. The final sintered powder was manually ground to a fine powder for characterization studies. Compared to a conventional single-step sintering process, the two-step method offers the advantage of minimizing impurity phases and enhancing reproducibility of the luminescent properties, which is critical for achieving reliable optical thermometry performance.[19]

Characterization

Structural and morphological characterization

X-ray diffraction (XRD) measurements were performed to determine the crystal structure and assess phase purity of the synthesized samples. Diffraction patterns were recorded on a PANalytical X'Pert PRO diffractometer using Cu Kα radiation (λ = 1.5406 Å) over a 2θ angular range of 10–80° with a step size of 0.02° and a counting time of 2 seconds per step. Phase identification and crystal structure refinement were conducted using the ICDD PDF-4 database and Rietveld refinement analysis. Scanning electron microscopy (SEM) was employed to investigate the morphological characteristics and microstructural features of the phosphor particles. Micrographs were acquired using a Hitachi SU-4800 field-emission scanning electron microscope operated at an accelerating voltage of 15 kV. Prior to analysis, samples were mounted on aluminum stubs and sputter-coated with a 10 nm gold layer to enhance surface conductivity and imaging contrast.

Optical characterization

Ultraviolet-visible-near-infrared (UV-Vis-NIR) absorption spectra were recorded in the wavelength range of 200–2500 nm using a PerkinElmer Lambda 365 spectrophotometer equipped with a diffuse reflectance accessory. Upconversion luminescence spectra were systematically acquired under 975 nm continuous-wave excitation provided by a frequency-doubled Spectra Physics 3900S tunable Ti:sapphire laser operated at a fixed excitation power density of 15 W cm^{-2}. The upconversion emission signals were collected *via* a high-resolution Avantes AvaSpec-ULS2048 CCD detector with a spectral resolution of 0.5 nm and an integration time of 1 second, with spectral data processed using AvaSoft evaluation software.

Temperature-dependent measurements

Temperature-dependent fluorescence intensity measurements were conducted by heating the phosphor samples from 298 K to 573 K using a Linkam THMS600 heating stage with a temperature stability of ±0.1 K. Upconversion spectra were systematically recorded at 25 K intervals to ensure comprehensive

thermal response characterization. The fluorescence intensity ratios (FIR) were calculated for four distinct emission bands (700, 470, 660, and 550 nm) to determine thermal sensitivity and temperature uncertainty parameters.

Optical penetration and attenuation through turbid media

To evaluate the optical penetration capability and signal attenuation behavior under strongly absorbing and scattering conditions, the LCLMO:Ho^{3+}/Tm^{3+}/Yb^{3+} phosphor was investigated under 975 nm excitation using the aforementioned Spectra Physics 3900S Ti:sapphire laser with an excitation power density of 15 W cm^{-2}. The near-infrared emission corresponding to the $^3H_4 \rightarrow {}^3H_6$ transition ($\approx$800 nm) was selectively collected through a standardized optically turbid overlayer (1 mm path length, optical density $\sim$0.2 at 975 nm). The emission intensity was systematically recorded as a function of overlayer thickness (0–5 mm in 0.5 mm increments) using a cooled Newton DU920N back-illuminated CCD detector with a spectral resolution of 0.7 nm, an integration time of 1 s per measurement point, and full vertical binning to optimize signal collection efficiency. All optical measurements were performed under ambient conditions (298 K, 1 atm) with appropriate dark-noise subtraction protocols.

Results and discussion

(1) Characterization structural and morphology:

To establish the compositional accuracy and morphological characteristics of the synthesized phosphors, the LCLMO:Ho^{3+}/Tm^{3+}/Yb^{3+} samples were subjected to comprehensive analytical examination. X-ray diffraction analysis was employed to determine the crystal structure and assess phase purity, as presented in Fig. 1a. All reflections matched well with the standard diffraction pattern for tetragonal $LiCaLa(MoO_4)_3$ (JCPDS #29-0351), confirming the formation of a highly crystalline material with an ordered single-phase structure.[19] The incorporation of Ho^{3+}, Tm^{3+}, and Yb^{3+} dopant ions does not significantly alter the host lattice structure, as evidenced by the conservation of the main crystallographic reflections and the absence of secondary phases, indicating successful substitution within the LCLMO framework without phase destabilization.

Rietveld refinement Fig. S1 was performed to refine the crystallographic parameters. The optimized unit cell dimensions are: $a = b = 5.25094$ Å, $c = 11.48446$ Å, and the unit cell volume = 317.53 $Å^3$. The refinement confirms a pure tetragonal phase with R-factors (R_p = 3.4%, R_{wp} = 4.2%) indicative of a high-quality fit. No detectable impurities or structural defects were observed, corroborating the effectiveness of the solid-state synthesis route.

Scanning electron microscopy was performed to examine the morphological features and particle size distribution of the synthesized phosphor, with representative micrographs presented in Fig. 1b. The SEM image reveals that the LCLMO:Ho^{3+}/Tm^{3+}/Yb^{3+} particles form agglomerated microstructures on the substrate, composed of individual crystallites with an average diameter of approximately 0.2–0.5 μm. The formation of agglomerated structures is typical for solid-state synthesized materials and arises from particle coalescence during the high-temperature sintering process. Although this agglomeration may result in some reduction of the active particle surface area compared to isolated spherical particles, the high crystallinity and excellent optical properties observed in subsequent luminescence characterization (as discussed below) demonstrate that the material's photoluminescent performance is not adversely compromised by this morphological feature.

(2) Optical characterization:

Fig. 2 presents the diffuse reflectance spectrum of LCLMO:Ho^{3+}/Tm^{3+}/Yb^{3+} recorded over the 200–1100 nm spectral range. The spectrum displays a prominent absorption band centered at 280 nm, which originates from the $O^{2-} \rightarrow Mo^{6+}$ charge-transfer transition within the MoO_4^{2-} polyanionic groups.[20] The characteristic absorption peaks of Tm^{3+} are clearly identified at 472 nm ($^1G_4 \rightarrow {}^3H_6$) and 795 nm ($^3H_4 \rightarrow {}^3H_6$) transitions, confirming the successful incorporation of thulium ions into the host matrix.[21] Additionally, two well-defined absorption features at 545 nm ($^5S_2 \rightarrow {}^5I_8$) and 655 nm ($^5F_5 \rightarrow {}^5I_8$) correspond to characteristic electronic transitions of Ho^{3+} ions.[22] Furthermore, a broad absorption band centered near 975 nm is assigned to the $^2F_{7/2} \rightarrow {}^2F_{5/2}$ transition of

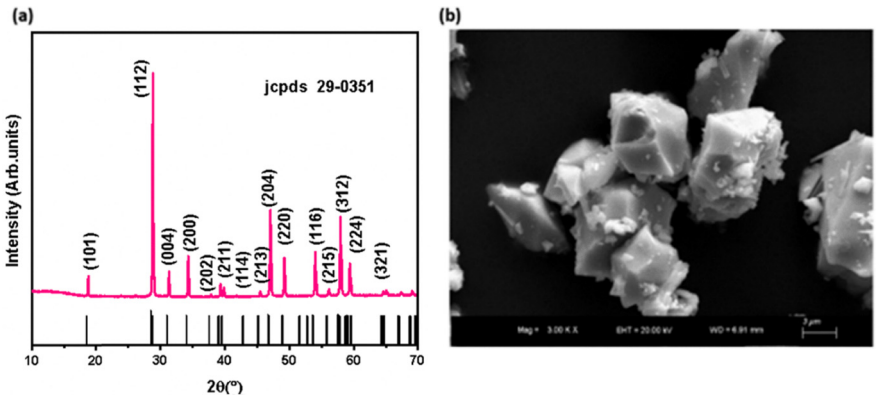

Fig. 1 (a) X-ray diffraction (XRD) pattern and (b) scanning electron microscopy (SEM) image of LCLMO:Ho^{3+}/Tm^{3+}/Yb^{3+} phosphor.

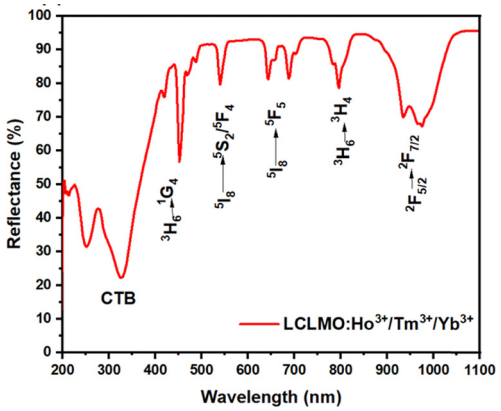

Fig. 2 Diffuse reflectance spectrum of LCLMO:Ho^{3+}/Tm^{3+}/Yb^{3+} phosphor recorded over the 200–1100 nm spectral range.

Yb^{3+}, the primary excitation transition for upconversion luminescence.[23]

Photoluminescence at room temperature

Fig. 3a displays the upconversion (UC) emission spectrum of LCLMO:Ho^{3+}/Tm^{3+}/Yb^{3+} phosphor under 975 nm excitation, revealing multiple emission bands spanning both the visible and near-infrared spectral regions. The blue emission band centered at 477 nm is attributed to the $^1G_4 \rightarrow {}^3H_6$ transition of Tm^{3+} ions.[24–27] The prominent visible emission peaks at 544 nm and 660 nm correspond to the $^5F_4$, $^5S_2 \rightarrow {}^5I_8$ and $^5F_5 \rightarrow {}^5I_8$ transitions of Ho^{3+} ions, respectively. Additionally, a notable emission band in the near-infrared region at approximately 795 nm is associated with the $^3H_4 \rightarrow {}^3H_6$ transition of Tm^{3+} ions.

Color coordinate analysis

To characterize the emission color properties of LCLMO:Ho^{3+}/Tm^{3+}/Yb^{3+} phosphors under 975 nm excitation, the Commission Internationale de l'Éclairage (CIE) 1931 color coordinate system was employed. Fig. 3b presents the CIE chromaticity coordinates obtained at room temperature (298 K). The measured CIE coordinates of ($x = 0.468$, $y = 0.407$) are located in the yellow-orange region of the CIE diagram, corresponding to a correlated color temperature (CCT) of approximately 2550 K, which confirms the warm emission characteristics of the phosphor. The CCT value was calculated using McCamy's empirical formula.[28]

Pump-power dependence and photon absorption analysis

The upconversion emission mechanisms and photon absorption pathways were investigated through pump-power dependent measurements of the UC luminescence intensities in LCLMO: Ho^{3+}/Tm^{3+}/Yb^{3+} phosphor, as illustrated in Fig. 4a. The number of photons involved in the upconversion process can be quantitatively determined using the power-law relationship:[29,30]

$$I = K \times P^n \quad (1)$$

where I is the emission intensity, P is the incident laser pump power, K is a proportionality constant, and n is the number of photons required to populate the emitting excited states. Analysis of the pump-power dependence yielded the following photon numbers: $n = 1.72$ for the 544 nm emission (Ho^{3+}, $^5F_4$, $^5S_2 \rightarrow {}^5I_8$), and $n = 1.32$ for the 660 nm emission (Ho^{3+}, $^5F_5 \rightarrow {}^5I_8$). These n values indicate that the Ho^{3+} emissions arise primarily from two-photon upconversion processes. For Tm^{3+} ions, the blue emission at 477 nm exhibits $n = 2.16$, suggesting a three-photon upconversion pathway, whereas the near-infrared emission at 795 nm displays $n = 1.47$, indicating a predominantly two-photon absorption mechanism.

Energy transfer mechanisms and upconversion processes

The electronic energy level structures of Tm^{3+}, Ho^{3+}, and Yb^{3+} ions and the corresponding upconversion emission mechanisms are illustrated in Fig. 4b. Under 975 nm laser excitation, the Yb^{3+} sensitizer ions absorb photons and populate the excited $^2F_{5/2}$ state, which serves as the primary energy donor to both Tm^{3+} and Ho^{3+} activator ions. In the Fig. S2 is shown the temporal dependence of the upconversion under pulse excitation at 975 nm. As can be seen, a curve with a rise time is obtained that indicates that different transfer processes are necessary to populate the green emitting level. In conclusion, the ET mechanism is the predominant instead the ESA process.

For Tm^{3+} ions, the upconversion process proceeds through sequential energy transfer steps. In the initial stage,

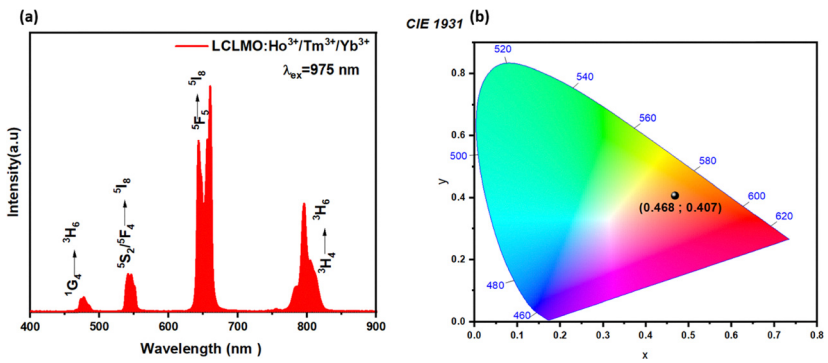

Fig. 3 (a) Upconversion emission spectrum of LCLMO:Ho^{3+}/Tm^{3+}/Yb^{3+} phosphor under 975 nm, (b) Commission Internationale de l'Éclairage (CIE) 1931 chromaticity diagram.

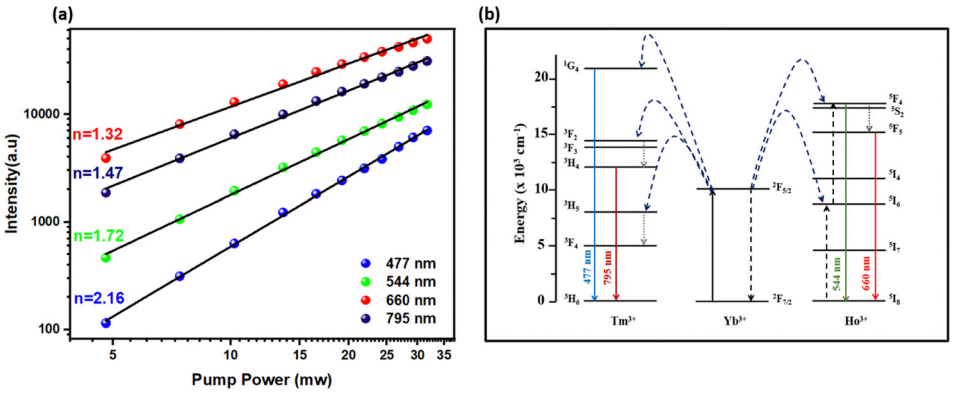

Fig. 4 (a) Upconversion emission intensity of LCLMO:Ho^{3+}/Tm^{3+}/Yb^{3+} phosphor as a function of incident pump power under 975 nm excitation, (b) schematic energy level diagram of Ho^{3+}, Tm^{3+}, and Yb^{3+} ions illustrating the upconversion mechanisms in the LCLMO host matrix.

ground-state Tm^{3+} ions in the $^3H_6$ level are excited *via* energy transfer from Yb^{3+} ($^2F_{5/2}$) to populate the $^3H_5$ state. These excited electrons subsequently undergo non-radiative relaxation to the $^3F_4$ level. From the $^3F_4$ state, Tm^{3+} ions absorb energy from a second excited Yb^{3+} ion ($^2F_{5/2}$), promoting them to the $^3F_2$ level. Non-radiative decay from the $^3F_2$ level proceeds sequentially through the intermediate $^3F_3$ and $^3H_4$ states. From the $^3H_4$ level, electrons can undergo radiative relaxation directly to the ground $^3H_6$ state, producing the characteristic near-infrared emission at 795 nm ($^3H_4 \rightarrow {}^3H_6$). Alternatively, from the $^3H_4$ level, further excitation *via* energy transfer from Yb^{3+} can populate the higher-energy $^1G_4$ state. Radiative transition from the $^1G_4$ level to the ground $^3H_6$ state generates the blue emission at 477 nm ($^1G_4 \rightarrow {}^3H_6$).[24,25]

For Ho^{3+} ions, the upconversion mechanism similarly involves sequential two-photon absorption processes. Ground-state Ho^{3+} ions in the $^5I_8$ level are initially excited *via* energy transfer from the Yb^{3+} ($^2F_{5/2}$) state to populate the $^5I_6$ excited state. Subsequently, Ho^{3+} ions in the $^5I_6$ state absorb energy from a second excited Yb^{3+} ion, undergoing further promotion to the $^5F_4/^5S_2$ level. From this intermediate state, radiative relaxation to the ground $^5I_8$ state generates the characteristic green emission at 544 nm ($^5F_4$, $^5S_2 \rightarrow {}^5I_8$). Additionally, non-radiative decay from the $^5F_4/^5S_2$ level to the $^5F_5$ state is followed by radiative transition ($^5F_5 \rightarrow {}^5I_8$), producing the red emission at 660 nm. The efficient energy transfer between Yb^{3+} sensitizers and Ho^{3+}/Tm^{3+} activators, combined with the low phonon energy of the LCLMO host matrix, enables high-efficiency upconversion luminescence across the visible and near-infrared spectral regions.[26,27,31]

Thermal sensing performance at high-temperature

The temperature dependence of the upconversion (UC) emission spectra of LCLMO:Ho^{3+}/Tm^{3+}/Yb^{3+} phosphor under 975 nm excitation across the temperature range of 298–588 K is presented in Fig. 5a. All fluorescence emission bands display pronounced temperature dependence. Notably, the emission at 700 nm, originating from the $^3F_{2,3} \rightarrow {}^3H_6$ electronic transition of Tm^{3+} ions, exhibits a systematic increase in integrated intensity with increasing temperature.[32] This temperature-induced enhancement of the 700 nm emission arises from the thermal population redistribution of Tm^{3+} ions among the closely-spaced $^3H_4$ and $^3F_{2,3}$ energy levels under thermal excitation, governed by Boltzmann's thermal distribution law. The Commission Internationale de l'Éclairage (CIE) chromaticity coordinates of the total emission were systematically measured

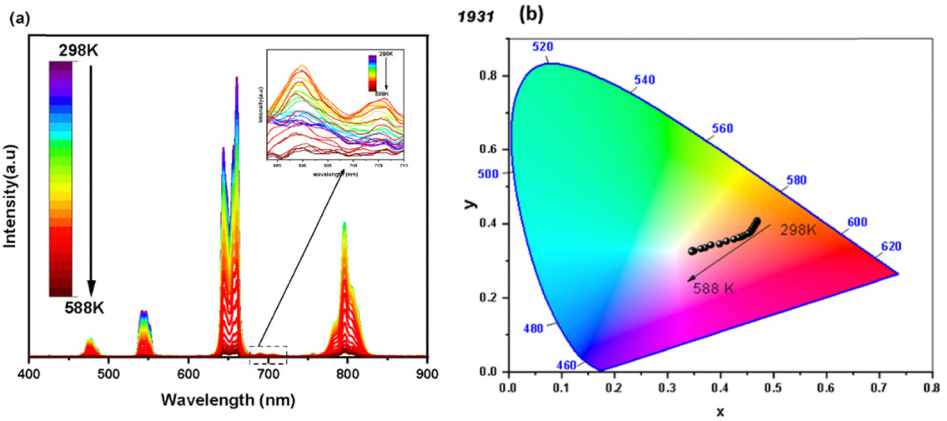

Fig. 5 (a) Temperature-dependent upconversion emission spectra of LCLMO:Ho^{3+}/Tm^{3+}/Yb^{3+} phosphor under 975 nm excitation recorded across the temperature range 298–588 K (b) Commission Internationale de l'Éclairage (CIE) 1931 chromaticity diagram.

as a function of temperature. As illustrated in Fig. 5b, the CIE coordinates, initially positioned in the orange region at room temperature (298 K), shift from (x = 0.468, y = 0.408) to (x = 0.345, y = 0.324) at 588 K. This systematic shift of the chromaticity coordinates reflects the temperature-induced variation in the relative emission intensities of individual spectral components, resulting in a measurable change in the overall emission color profile.

Luminescent thermometry methodology

To establish quantitative thermometric performance parameters, this study exploited the dual emission centers of Tm^{3+} and Ho^{3+} ions, which possess thermally sensitive excited states.[33] Two complementary approaches were employed: (1) thermally coupled level pairs (TCL), utilizing the 700 nm ($^3F_{2,3} \rightarrow {}^3H_6$) and 795 nm ($^3H_4 \rightarrow {}^3H_6$) emissions from Tm^{3+}, which originate from closely-spaced electronic states; and (2) non-thermally coupled level pairs (NTCL), employing multiple ratiometric combinations: 700 nm/470 nm, 700 nm/660 nm, and 700 nm/550 nm, which involve transitions between non-adjacent energy levels.

The fluorescence intensity ratio (FIR) between two thermally coupled levels follows Boltzmann's statistical distribution, as described in the following relationship:[34]

$$\mathrm{FIR_{TCL}} = \frac{I_{700}}{I_{795}} = A\exp\left(-\frac{\Delta E}{k_B T}\right) \quad (2)$$

where I_{700} and I_{795} are the UC intensities of the $^3F_{2,3} \rightarrow {}^3H_6$ and $^3H_4 \rightarrow {}^3H_6$ transitions, A is a constant, ΔE is the energy gap between the $^3F_{2,3}$ and $^3H_4$ levels, k_B is the Boltzmann constant, and T is the absolute temperature.

In the case of NTCL, it is difficult to be distributed by thermal excitation due to its large energy gaps. Therefore, the traditional FIR is not suitable for NTCL. The experimental FIR can be well fitted by the well-known Boltzmann distribution law with an offset constant C given by the formula:[21]

$$\mathrm{FIR_{NTCL}} = \frac{I_1}{I_2} = A\exp\left(-\frac{\Delta E}{k_B T}\right) + C \quad (3)$$

Panels (a–d) of Fig. 6 display the temperature dependence of the fluorescence intensity ratios $FIR_{700/795}$, $FIR_{700/477}$, $FIR_{700/550}$, $FIR_{700/660}$ for LCLMO:Ho^{3+}/Tm^{3+}/Yb^{3+} phosphor. The fitting results for each fluorescence intensity ratio demonstrate excellent agreement with the experimental data, confirming the applicability of the thermal sensing model. The absolute sensitivity (S_a) and relative sensitivity (S_r) represent critical thermometric performance parameters that quantitatively evaluate the material's temperature sensing capability. These parameters can be mathematically expressed according to the following relationships:[35]

$$S_a = \frac{\partial \mathrm{FIR}}{\partial T} \quad (4)$$

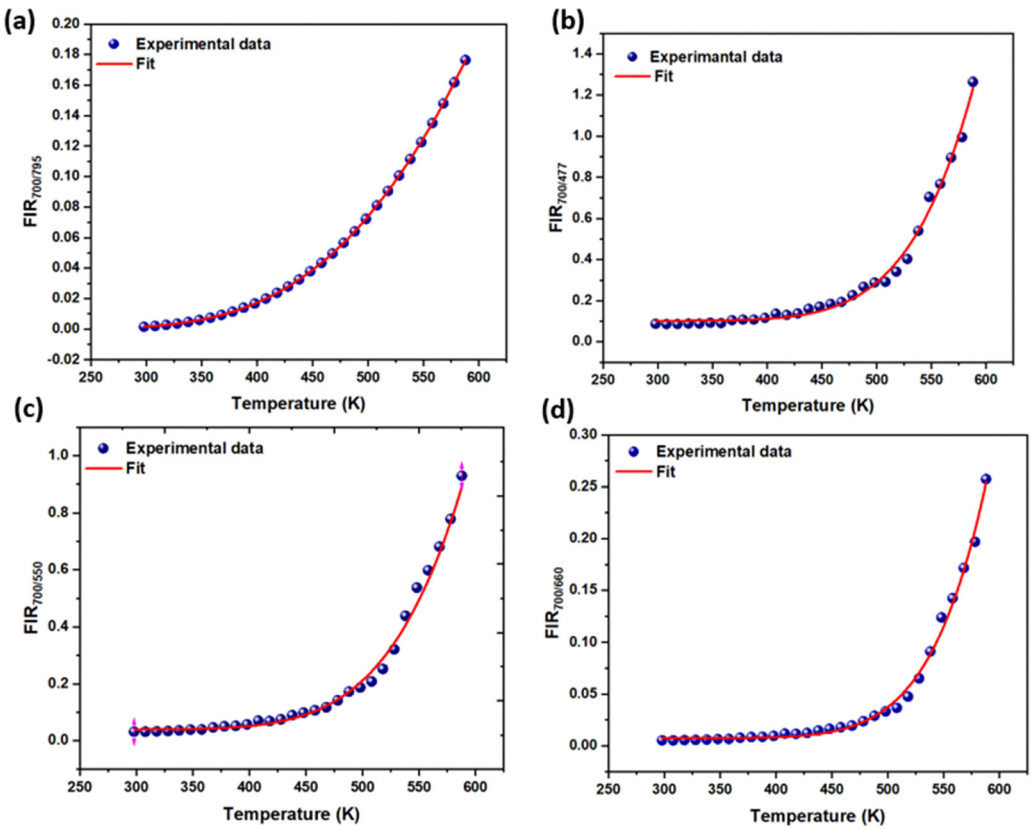

Fig. 6 Fluorescence intensity ratio (FIR) as a function of temperature for LCLMO:Ho^{3+}/Tm^{3+}/Yb^{3+} phosphor: (a) $FIR_{700/795}$ (TCL), (b) $FIR_{700/477}$, (c) $FIR_{700/550}$, and (d) $FIR_{700/660}$ (NTCL) measured across the 298–588 K temperature range.

$$S_r = \frac{1}{FIR} \times \frac{\partial FIR}{\partial T} \times 100\% \quad (5)$$

Fig. 7 displays the temperature dependence of the absolute and relative sensitivities for all investigated fluorescence intensity ratio pairs. For the thermally coupled Tm^{3+} levels ($FIR_{700/795}$), the relative sensitivity (S_r) decreases monotonically with increasing temperature, reaching a maximum value of $S_r(max)$ = 3.22% K^{-1} at the lowest temperature (298 K). In contrast, the absolute sensitivity (S_a) increases with rising temperature, attaining a value of $S_a = 1.4 \times 10^{-3}$ K^{-1} at the upper temperature limit.

For the non-thermally coupled pair ($FIR_{700/477}$) involving a single Tm^{3+} center, the relative sensitivity exhibits an inverse trend, increasing progressively with temperature and reaching a maximum of $S_r(max)$ = 1.7% K^{-1} at 540 K. Conversely, the absolute sensitivity S_a continues to increase throughout the measured temperature range, attaining a maximum of $S_a(max) = 5.0 \times 10^{-3}$ K^{-1} at 588 K.

For non-thermally coupled transitions involving two emitting centers (Ho^{3+} and Tm^{3+}), distinct thermal behaviors are observed. The $FIR_{700/550}$ pair exhibits an increase in relative sensitivity reaching $S_r(max)$ = 1.5% K^{-1} at 520 K, with absolute sensitivity attaining $S_a = 1.2 \times 10^{-2}$ K^{-1}. The $FIR_{700/660}$ pair demonstrates a continuous increase in relative sensitivity with temperature, reaching $S_r(max)$ = 2.23% K^{-1} at 500 K, while the absolute sensitivity achieves $S_a = 5.0 \times 10^{-3}$ K^{-1}.

Comprehensive analysis of all investigated FIR pairs clearly demonstrates that the thermally coupled level configuration ($FIR_{700/795}$) exhibits the highest relative sensitivity, with $S_r(max) \approx 3.22\%$ K^{-1}, approximately 1.9 times higher than the best-performing non-thermally coupled pair ($FIR_{700/660}$). This exceptional thermal sensitivity, combined with outstanding temperature measurement accuracy and non-invasive nature, establishes the LCLMO:Ho^{3+}/Tm^{3+}/Yb^{3+} phosphor utilizing the $FIR_{700/795}$ as the optimal configuration for precise luminescent thermometry applications. Table 1 provides a comprehensive comparison of the maximum relative temperature sensitivity $S_r(max)$ of LCLMO:Ho^{3+}/Tm^{3+}/Yb^{3+} with other lanthanide-doped phosphor hosts reported in the literature, demonstrating that the developed thermometer achieves exceptional performance across an extended temperature range (up to 588 K), with particular utility in high-temperature industrial and biomedical diagnostic applications.

Experimental temperature uncertainty and limit of detection

To quantitatively evaluate the minimum detectable temperature variation and establish the experimental temperature uncertainty (limit of detection, LOD) for the optical thermometer, 60 consecutive upconversion emission spectra were systematically recorded at a fixed reference temperature of 300 K. This statistical sampling approach allows determination of the measurement precision and repeatability inherent to each fluorescence intensity ratio (FIR) thermometer. Temperature estimates derived from these repeated measurements were calculated for all four FIR configurations and analyzed for statistical distribution.

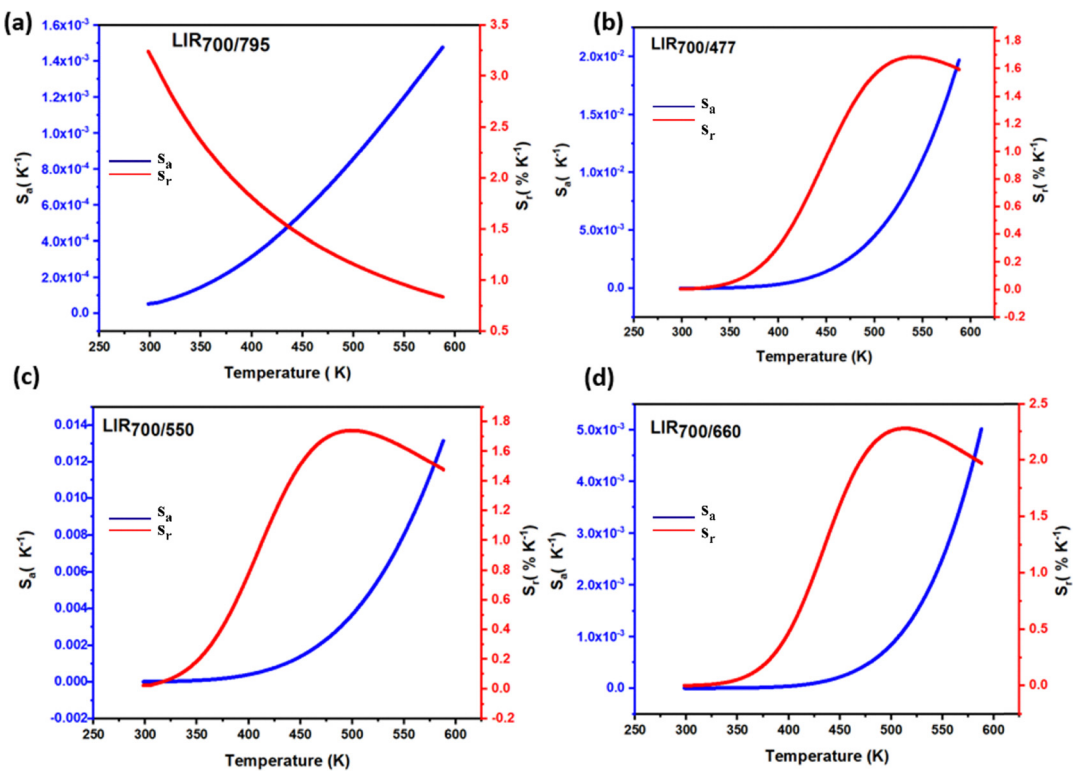

Fig. 7 Temperature-dependent absolute sensitivity (S_a) and relative sensitivity (S_r) values calculated for LCLMO:Ho^{3+}/Tm^{3+}/Yb^{3+} phosphor (a) $FIR_{700/795}$ (TCL), (b) $FIR_{700/477}$, (c) $FIR_{700/550}$, and (d) $FIR_{700/660}$ (NTCL) measured across the 298–588 K temperature range.

Table 1 Comparative analysis of optical temperature sensing properties of lanthanide-doped phosphor thermometric materials

Materials	Excitation wavelength (nm)	FIR (nm)	S_r(max) (% K^{-1})	T range (K)	Ref.
$LiNdO_3$:Tm^{3+}/Yb^{3+}	980	700/476	0.70	323–773	36
Y_2WO_6:Ho^{3+}/Yb^{3+}	980	662/540	0.61	293–513	37
$Ba_3Y_4O_9$:Ho^{3+}/Tm^{3+}/Yb^{3+}	980	803/482	0.34	298–573	38
Y_2O_2:Ho^{3+}/Yb^{3+}	976	540/660	1.03	298–473	39
$BaIn_2O_4$:Ho^{3+}/Tm^{3+}/Yb^{3+}	980	550/666	0.44	353–473	40
$KLu(WO_3)_2$:Ho^{3+}/Tm^{3+}/Yb^{3+}	980	696/545	0.60	273–523	41
LCLMO:Ho^{3+}/Tm^{3+}/Yb^{3+}	975	700/795	3.22	298–588	This work
LCLMO:Ho^{3+}/Tm^{3+}/Yb^{3+}	975	700/477	1.70	298–588	This work
LCLMO:Ho^{3+}/Tm^{3+}/Yb^{3+}	975	700/550	1.50	298–588	This work
LCLMO:Ho^{3+}/Tm^{3+}/Yb^{3+}	975	700/660	2.23	298–588	This work

The temperature values obtained from the 60 consecutive spectra at 300 K exhibited Gaussian probability distributions, as illustrated in Fig. 8(a)–(d). The remarkably low temperature uncertainty values, particularly the exceptional precision of the $FIR_{700/795}$ (the lowest at 0.8 K), directly reflect the high signal-to-noise ratio and excellent reproducibility of the optical system and spectral data acquisition.

Performance assessment and implications

The superior measurement precision demonstrated by the LCLMO:Ho^{3+}/Tm^{3+}/Yb^{3+} optical thermometer, with minimum temperature uncertainty (ΔT_{min} = 0.8 K), confirms its outstanding stability and exceptional detection capability. The thermally coupled level pair $FIR_{700/795}$ exhibits both the highest relative sensitivity (S_r(max) = 3.22% K^{-1}) and the lowest measurement uncertainty, establishing it as the optimal configuration for precision temperature sensing. The combination of high thermal sensitivity, minimal measurement error, and extended temperature measurement range (298–588 K) demonstrates that LCLMO:Ho^{3+}/Tm^{3+}/Yb^{3+} phosphors fulfill the stringent requirements for non-invasive, real-time, high-resolution thermal mapping in high-temperature industrial process monitoring applications.

Experimental setup and optical attenuation methodology

To evaluate the optical penetration performance of LCLMO: Ho^{3+}/Tm^{3+}/Yb^{3+} phosphors under conditions representative of highly absorbing and scattering media, a simple and reproducible vertical optical configuration was employed (Fig. 9). In this setup, a quartz cuvette filled with an optically turbid medium was positioned directly above a sample holder containing the phosphor material, ensuring a well-defined

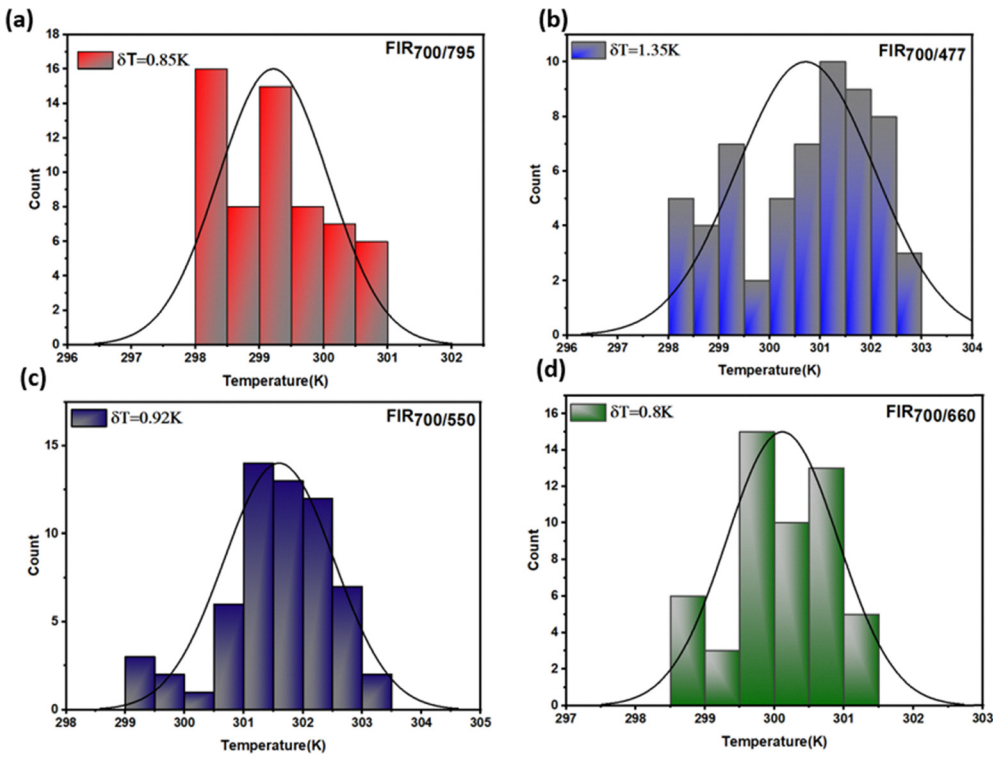

Fig. 8 Histograms of temperature distribution obtained from 60 repeated measurements at room temperature (300 K) using the fluorescence intensity ratios of LCLMO:Ho^{3+}/Tm^{3+}/Yb^{3+} phosphor: (a) $FIR_{700/795}$, (b) $FIR_{700/477}$, (c) $FIR_{700/550}$, and (d) $FIR_{700/660}$.

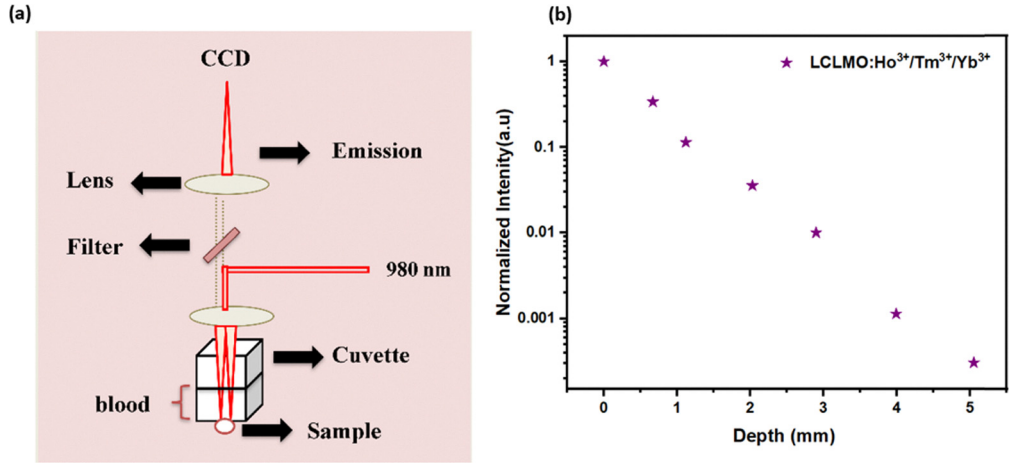

Fig. 9 (a) Schematic diagram of the experimental setup used to evaluate optical penetration through an optically attenuating (absorbing/scattering) medium, showing the vertical optical geometry with 975 nm laser excitation directed through a quartz cuvette positioned above the LCLMO:$Ho^{3+}/Tm^{3+}/Yb^{3+}$ phosphor sample. (b) Luminescence intensity as a function of overlayer thickness for the near-infrared emission at 800 nm (Tm^{3+} $^3H_4 \rightarrow {}^3H_6$ transition).

excitation and emission collection geometry suitable for practical optical sensing conditions.

Upon continuous-wave excitation at 975 nm, the near-infrared emission centered at approximately 800 nm, corresponding to the Tm^{3+} ($^3H_4 \rightarrow {}^3H_6$) transition, was monitored as a function of increasing overlayer thickness. As expected from fundamental light–matter interaction mechanisms, the detected luminescence intensity exhibited an exponential attenuation with increasing layer thickness, primarily due to the combined effects of absorption and elastic/inelastic scattering within the turbid medium.[42]

In our previously reported work on a related LCLMO-based host system,[21] an optical penetration depth of approximately 4 mm was observed in the near-infrared spectral range (650–1000 nm) using a binary lanthanide-doped composition. In the present $Ho^{3+}/Tm^{3+}/Yb^{3+}$ tri-doped system, a detectable near-infrared luminescence signal is sustained up to an overlayer thickness of approximately 5 mm in an optically complex and strongly attenuating medium, corresponding to an improvement of about 25% compared to the binary system. This enhancement is attributed to the introduction of Ho^{3+} as an additional emitting center, which strengthens near-infrared emission and facilitates signal propagation through highly absorbing and scattering environments.

From an optical standpoint, the ability to maintain detectable near-infrared emission over several millimeters of an optically turbid overlayer highlights the favorable photophysical properties of the LCLMO molybdate host lattice under realistic excitation/collection constraints.[43] When combined with the high ratiometric thermometric performance demonstrated earlier, these findings suggest that the material system can serve as a robust proof-of-concept optical platform for multifunctional luminescent sensing.

It is important to emphasize that the attenuating medium employed here serves as a practical model to assess light attenuation and penetration characteristics, rather than to demonstrate biological compatibility or *in vivo* applicability. Therefore, no conclusions regarding cytotoxicity, biocompatibility, aqueous stability, or photothermal safety can be drawn from these experiments.

Conclusion

In conclusion, this work demonstrates the successful synthesis and comprehensive optical characterization of $Ho^{3+}/Tm^{3+}/Yb^{3+}$ tri-doped $LiCaLa(MoO_4)_3$ (LCLMO) phosphors as a luminescent platform for ratiometric optical thermometry. The favorable characteristics of the LCLMO host lattice including high thermal stability, low phonon energy, and a tunable crystal field environment enable efficient energy transfer processes among Yb^{3+} sensitizers and Ho^{3+}/Tm^{3+} activators, resulting in intense and stable upconversion emissions. Thermometric performance evaluated using four optimized fluorescence intensity ratio channels, comprising one thermally coupled ($FIR_{700/795}$) and three non-thermally coupled pairs ($FIR_{700/477}$, $FIR_{700/550}$, and $FIR_{700/660}$), yields a high relative sensitivity of 3.22% K^{-1} at 298 K along with excellent temperature resolution (ΔT = 0.8 K) across a wide operating range of 298–588 K. Proof-of-concept optical penetration experiments conducted through a standardized optically turbid overlayer demonstrate detectable NIR emission up to an overlayer thickness of approximately 5 mm, representing a ~25% improvement over previously reported binary lanthanide-doped systems and highlighting the enhanced optical robustness of the tri-doped composition. The combined advantages of high thermometric sensitivity, multi-channel ratiometric reliability and extended temperature operability establish LCLMO:$Ho^{3+}/Tm^{3+}/Yb^{3+}$ phosphors as promising candidates for advanced luminescent thermometry, optical sensing, and multifunctional photonic applications.

Conflicts of interest

There are no conflicts to declare.

Data availability

Supplementary information (SI): Fig. S1. Rietveld refinement of the XRD pattern of LCLMO:Ho^{3+}/Tm^{3+}/Yb^{3+}. Fig. S2. Time-resolved upconversion emission of LCLMO:Ho^{3+}/Tm^{3+}/Yb^{3+} under 975 nm pulsed excitation. See DOI: https://doi.org/10.1039/d6ma00079g.

All data underlying the results are available as part of the article and no additional source data are required.

References

1 J. Xue, H. M. Noh, B. C. Choi, S. H. Park, J. H. Kim, J. H. Jeong and P. Du, *Chem. Eng. J.*, 2020, **382**, 122861, DOI: 10.1016/j.cej.2019.122861.
2 J. Zhu, T. Yang, H. Li, Y. Xiang, R. Song, H. Zhang and B. Wang, *SSRN Electr. J.*, 2023, 4420994, DOI: 10.2139/ssrn.4420994.
3 B. Hou, M. Jia, P. Li, G. Liu, Z. Sun and Z. Fu, *Inorg. Chem.*, 2019, **58**, 7939–7946.
4 M. Dong, T. Yin, G. Guo, Z. Liu, F. Wang, C. Wang, L. Guan and X. Li, *Ceram. Int.*, 2024, **50**, 1050–1058.
5 K. Li, D. Zhu and H. Lian, *J. Alloys Compd.*, 2020, **816**, 152554.
6 N. Ben Amar, K. Saidi, C. Hernández-Álvarez, M. Dammak and I. R. Martín, *ACS Appl. Nano Mater.*, 2025, **8**(35), 17133–17143.
7 X. Wang, Q. Liu, Y. Bu, C. S. Liu, T. Liu and X. Yan, *RSC Adv.*, 2015, **5**, 86585–86601.
8 Y. Gao, F. Huang, H. Lin, J. Xu and Y. Wang, *Sens. Actuators, B*, 2017, **243**, 137–144.
9 S. Liu, T. Zhao, R. Abdurahman, X. Yang, Y. Han, Y. Zhang and X.-B. Yin, *J. Alloys Compd.*, 2025, **1010**, 177815.
10 M. Runowski, P. Woźny, I. R. Martín, V. Lavín and S. Lis, *J. Lumin.*, 2019, **214**, 116571.
11 M. Runowski, A. Bartkowiak, M. Majewska, I. R. Martín and S. Lis, *J. Lumin.*, 2018, **201**, 104–109.
12 Z. E. A. A. Taleb, K. Saidi and M. Dammak, *RSC Adv.*, 2024, **14**(12), 8366–8377.
13 N. B. Amar, K. Saidi, C. Hernández-Álvarez, M. Dammak and I. R. Martin, *Mater. Adv.*, 2025, **6**, 827–838.
14 M. Xing, T. Pang, L. Yan, L. Kang, X. Wu, H. Wang, Y. Fu, X. Luo and Y. Tian, *Mater. Today Chem.*, 2023, **27**, 101304.
15 P. Guo, J. Wang, C. Liao, H. Zhou, D. Huang, G. Zhou, X. Yu and J. Hu, *RSC Adv.*, 2022, **12**, 33419–33427.
16 G. B. Nair, S. Tamboli, S. J. Dhoble and H. C. Swart, *ACS Appl. Nano Mater.*, 2023, **6**, 15255.
17 J. Grigorjevaite and A. Katelnikovas, *Materials*, 2023, **16**, 917.
18 K. Li, Z. Zhang, D. Zhu and C. Yue, *Inorg. Chem. Front.*, 2024, **11**, 7464.
19 P. Sharma, J. P. Madda and S. Vaidyanathan, *Dalton Trans.*, 2023, **52**, 15043.
20 Y. Bahrouni, I. Kachou, K. Saidi, T. Kallel, M. Dammak, I. Mediavilla and J. Jiménez, *Mater. Adv.*, 2025, **6**, 1307–1318.
21 I. Kachou, K. Saidi, Z. E. A. A. Taleb, C. Hernández-Álvarez, M. Dammak and I. R. Martín, *Mater. Adv.*, 2025, **6**, 5546–5556.
22 Y. Yang, Y. Yu, L. Feng, R. Li, Z. Ao, J. Zhang, Y. Sun and J. Liao, *Mater. Res. Bull.*, 2026, **197**, 113991.
23 F. Ren, C. Song, Y. Cong, Y. Wu, Y. Bai and D. Zhou, *Ceram. Int.*, 2023, **49**, 32850.
24 P. Guo, J. Wang, C. Liao, H. Zhou, D. Huang, G. Zhou, X. Yu and J. Hu, *RSC Adv.*, 2022, **12**, 33419–33427.
25 S. Singh, P. K. Vishwakarma, M. Sharma and S. K. Singh, *J. Mol. Struct.*, 2025, **1340**, 142452.
26 H. Lu, H. Hao, Y. Gao, D. Li, G. Shi, Y. Song, Y. Wang and X. Zhang, *Microchim. Acta*, 2017, **184**, 641–649.
27 V. Makumbane, M. Y. A. Yagoub, Z. Xia, R. E. Kroon and H. C. Swart, *Crystals*, 2023, **13**, 1288.
28 A. Pandey and V. K. Rai, *Appl. Phys. B:Lasers Opt.*, 2012, **109**, 611.
29 N. Q. Wang, X. Zhao, C. M. Li, E. Y. B. Pun and H. Lin, *J. Lumin.*, 2010, **130**, 1044.
30 Y. Pei, S. An, C. Zhuang, D. Sun, X. Li and J. Zhang, *J. Lumin.*, 2022, **250**, 119073.
31 P. Tadge, R. S. Yadav, P. K. Vishwakarma, S. B. Rai, T.-M. Chen, S. Sapra and S. Ray, *J. Alloys Compd.*, 2020, **821**, 153230.
32 M. Ding, M. Zhang and C. Lu, *Mater. Lett.*, 2017, **209**, 52–55.
33 H. Zhou, X. Liang, L. Zhang, F. Hu and H. Guo, *Opt. Mater.*, 2024, **157**, 116271.
34 I. Kachou, K. Saidi, Y. Bahrouni, C. Hernández-Álvarez, M. Dammak and I. R. Martín, *Ceram. Int.*, 2025, **51**, 61491–61502.
35 Q. Li, Z. Zhang and K. Li, *Ceram. Int.*, 2025, DOI: 10.1016/j.ceramint.2025.12.503.
36 L. Xing, R. Ao, Y. Liu and W. Yang, *Spectrochim. Acta, Part A*, 2019, **222**, 117159.
37 J. Zhang, B. Ji, G. Chen and Z. Hua, *Inorg. Chem.*, 2018, **57**, 5038–5045.
38 S. Liu, J. Cui, J. Jia, J. Fu, W. You, Q. Zeng, Y. Yang and X. Ye, *Ceram. Int.*, 2019, **45**, 1–8.
39 N. An, L. Ye, R. Bao, L. Yue and L.-G. Wang, *J. Lumin.*, 2019, **215**, 116657.
40 H. Liu, M. Liu, K. Wang, B. Wang, X. Jian, G. Bai and Y. Zhang, *Dalton Trans.*, 2021, **50**, 12107–12115.
41 O. A. Savchuk, J. J. Carvajal, M. C. Pujol, J. Massons, P. Haro-González, O. Martínez, J. Jiménez, M. Aguiló and F. Díaz, *J. Lumin.*, 2016, **169**, 711–720.
42 M. A. Hernández-Rodríguez, A. D. Lozano-Gorrín, I. R. Martín, U. R. Rodríguez-Mendoza and V. Lavín, *Sens. Actuators, B*, 2018, **255**, 970–976.
43 U. Rocha, C. Jacinto da Silva, W. F. Silva, I. Guedes, A. Benayas, L. Martínez Maestro, M. Acosta Elias, E. Bovero, F. C. J. M. van Veggel, J. A. García Solé and D. Jaque, *ACS Nano*, 2013, **7**, 1188–1199.